Atmos. Meas. Tech. Discuss., 6, 5577–5619, 2013
www.atmos-meas-tech-discuss.net/6/5577/2013/
doi:10.5194/amtd-6-5577-2013

Atmospheric Measurement Techniques Discussions

The identification and tracking of volcanic ash using the Meteosat Second Generation (MSG) Spinning Enhanced Visible and Infra-Red Imager (SEVIRI)

A. R. Naeger[1] **and S. A. Christopher**[1,2]

[1]Department of Atmospheric Sciences, UA Huntsville, 320 Sparkman Drive, Huntsville, AL 35805, USA
[2]Earth System Science Center, UA Huntsville, 320 Sparkman Drive, Huntsville, AL 35805, USA

Received: 10 May 2013 – Accepted: 11 June 2013 – Published: 21 June 2013

Correspondence to: A. R. Naeger (naeger@nsstc.uah.edu)

Published by Copernicus Publications on behalf of the European Geosciences Union.

Abstract

In this paper, we develop an algorithm based on combining spectral, spatial, and temporal thresholds from the geostationary Spinning Enhanced Visible and InfraRed Imager (SEVIRI) daytime measurements to identify and track different aerosol types, primarily volcanic ash. Contemporary methods typically do not use temporal information to identify ash. We focus not only on the identification and tracking of volcanic ash during the Eyjafjallajökull volcanic eruption period beginning 14 April 2010 to May but a pixel level classification method for separating various classes in the SEVIRI images. Three case studies on 19 April, 16 May, and 17 May are analyzed in extensive detail with other satellite data including the Moderate Resolution Imaging Spectroradiometer (MODIS), Multi-angle Imaging Spectroradiometer (MISR), Cloud-Aerosol Lidar and Infrared Pathfinder Satellite Observations (CALIPSO), and Facility for Airborne Atmospheric Measurements (FAAM) BAe146 aircraft data to verify the aerosol spatial distribution maps generated by the SEVIRI algorithm. Our results indicate that the SEVIRI algorithm is able to track volcanic ash even at these high latitudes. Furthermore, the BAe146 aircraft data shows that the SEVIRI algorithm detects nearly all ash regions when AOD > 0.2. However, the algorithm has higher uncertainties when AOD is < 0.1 over water and AOD < 0.2 over land. The ash spatial distributions provided by this algorithm can be used as a critical input and validation for atmospheric dispersion models simulated by Volcanic Ash Advisory Centers (VAACs). Identifying volcanic ash is an important first step before quantitative retrievals of ash concentration can be made.

1 Introduction

The Eyjafjallajökull volcano located on the southern coast of Iceland (63.6° N, 19.6° W) began emitting ash into the atmosphere on 14 April 2010. Although only a mid-size eruption (Mason et al., 2004; Mastin et al., 2009), the volcano had a tremendous impact on air traffic as the strong atmospheric winds transported the ash southeasterly

AMTD
6, 5577–5619, 2013

towards Europe (Ansmann et al., 2010a). By 16 April 2010, a dense ash plume was observed across Central Europe by Aerosol Robotic Network (AERONET) Sun photometers and ground based lidars (Ansmann et al., 2010b). The presence of dense ash caused nearly a week-long stoppage in air travel over many parts of Europe. Flight cancellations that occurred over the ensuing week proved extremely costly to the airline industry as monetary losses were over 1 billion US dollars. Also, the damaging effects of volcanic ash on commercial airplanes can be deadly due to their low melting temperature and sharp-edged shapes (Casadevall, 1992). Therefore, it is critical that we accurately track volcanic ash during an eruption period.

To track the spatial distribution of volcanic ash, satellite remote sensing is important as the spatial distribution of ash varies strongly especially after an eruption. Ground based stations are inadequate for understanding the spatial distribution as they only provide point measurements. Satellites are also an important tool for verifying models that predict ash concentrations and spatial distributions (Millington et al., 2012). These models are usually high resolution dispersion models that predict height dependent ash concentrations used by Volcanic Ash Advisory Centers (VAACs). Although polar orbiting satellites such as the Moderate Resolution Imaging Spectroradiometer (MODIS) can provide high spatial resolution of volcanic ash plumes (Sigmundsson et al., 2010), their temporal resolution is insufficient to track ash plumes being transported long distances over relatively short time scales. Thus, geostationary satellite sensors such as the Spinning Enhanced Visible and InfraRed Imager (SEVIRI) are critical for assessing the spatial distributions of ash due to their high temporal resolutions (Prata and Kerkmann, 2007; Christopher et al., 2012).

Ultimately it is important to know the vertical distribution of ash concentrations before important decisions can be made regarding commercial flights during eruptions. However the first task is to detect the volcanic ash on a pixel-by-pixel basis. The first limitation to note is the SEVIRI cannot detect ash below clouds which is a common issue for passive satellite data sets that operate in the visible to the infrared part of the electromagnetic spectrum. However the repeated temporal information and the large

AMTD
6, 5577–5619, 2013

spatial coverage make SEVIRI an excellent tool for mapping volcanic ash over large areas. The common method is to simply assign separate channels to the Red, Green, and Blue and visually examines the ash by looking for certain colors. This is often problematic since clouds can be confused as ash and not all aerosols appear to have the same color; and therefore, it is important to develop an algorithm that separates an image into various classes, such as cloud and aerosol, for further studies that may involve calculation of ash concentrations.

Prata (1989) presented a very commonly used technique that exploits the brightness temperature difference (BTD) between the 11 and 12 µm channels. The limitations with this simple technique are well known and discussed in Prata et al. (2001) where one major limitation is that high water vapor amounts can mask the negative BTD signal which the technique relies on ash detection. Pergola et al. (2004) developed a more sophisticated ash detection technique that compares a measured satellite signal to a reference field computed from long-term historical records. In particular, they use three channels centered at approximately 3.75, 11.0, and 12.0 µm from the Advanced Very High Resolution (AVHRR) to compute the reference fields and they show that this Robust AVHRR Technique (RAT) is more accurate in detecting volcanic ash than the simple BTD technique presented in Prata (1989). However, this approach requires multiple years of data over a region to compute the reference fields. Pavolonis et al. (2006) developed a four channel ash detection algorithm that utilizes the 0.65, 3.75, 11.0, and 12.0 µm channels and does not rely on a reference field but instead uses spectral tests and a spatial filtering routine. They showed that this four channel algorithm is much better at detecting volcanic ash regions compared to the BTD approach with less false detections. We take a different approach by developing an algorithm using SEVIRI measurements that exploits temporal thresholds along with spectral and spatial thresholds to classify each pixel into various classes (e.g., cloud, land, and aerosol). This algorithm uses seven different SEVIRI channels to produce detailed spatial distribution maps of cloud and aerosol.

AMTD
6, 5577–5619, 2013

Although the SEVIRI instrument is not equipped with near ultraviolet (UV) channels, it is important to note the ability of the near-UV channels in detecting volcanic ash. Torres et al. (1998) used the near-UV channels of 340 and 380 nm from the Total Ozone Mapping Spectrometer (TOMS) instrument to detect volcanic ash, and they found that these two channels have great success in detecting ash over snow/ice or above clouds. This is an important advantage of using the near-UV channels as detection techniques using channels from the visible to infrared spectrums, such as the RAT and our SEVIRI algorithm, do not possess the same capability of detecting ash over snow/ice or above clouds (Pergola et al., 2004). In addition, Krotkov et al. (1999) showed that the near-UV channels of the TOMS instrument can detect the optically opaque, very fresh ash which is often missed by the visible and infrared techniques.

This study tracks the ash plumes emitted from the Eyjafjallajökull volcano from its initial eruption on 14 April until the end of the eruption period on 23 May using the high temporal resolution measurements of SEVIRI onboard the Meteosat Second Generation (MSG-2) satellite. Since we use the visible along with the infrared channels of SEVIRI, the algorithm developed in this study can only track the ash plumes during the daylight periods for volcanic ash in cloud-free conditions. We present results from the SEVIRI algorithm throughout the eruption period but place special emphasis on six days in May 2010 when the Facility for Airborne Atmospheric Measurements (FAAM) BAe146 research aircraft measurements was available (Johnson et al., 2012). We use the FAAM BAe146 aircraft measurements as validation for the SEVIRI algorithm developed in this study. Other sources of verification data used in this study to assess the spatial distribution of the aerosols detected by the SEVIRI algorithm include the MODIS, the Multi-angle Imaging SpectroRadiometer (MISR), and the Cloud-Aerosol Lidar and Infrared Pathfinder Satellite Observation (CALIPSO).

AMTD
6, 5577–5619, 2013

2 Data

The goal of the paper is to develop a pixel level algorithm from SEVIRI reflectance and temperature measurements using temporal threshold tests along with spatial and spectral threshold tests. It is important to note that the retrieval of ash concentrations and aerosol particle size information is beyond the scope of this study. We have already noted that the use of temporal thresholds and some of the spatial thresholds used in this paper is not routinely done by standard algorithms (i.e., Prata, 1989). After classifying the volcanic ash pixels, we need to determine the accuracy of the algorithm but this is a difficult task to accomplish. We have chosen to intercompare the SEVIRI algorithm results with MODIS and MISR products by making the assumption that their identification is correct. We take this a step further by comparing our results with aircraft data but not many data points can be obtained with such a comparison. This is not a unique problem to our study since all validation methods have to use a verification source and then provide results and analysis.

Table 1 shows the SEVIRI channels with the center, minimum, and maximum wavelengths for each channel. These channels have a sampling distance of 3 km at subsatellite point (Schmetz et al., 2002). The channels used to develop the SEVIRI algorithm are highlighted while the channels ignored are primarily used for water vapor, ozone, and carbon dioxide detection. Thus, the SEVIRI algorithm uses three channels in the solar spectrum and four channels in the infrared spectrum.

The MODIS onboard the Terra and Aqua polar orbiter satellites have 36 channels over the spectral range from 0.4–14.4 µm with spatial resolutions of 250 m, 500 m, and 1 km (Savtchenko et al., 2004). A Level 2 aerosol optical thickness (AOT) operational product over both ocean and non bright land surfaces is provided by MODIS at a spatial resolution of 10 km (at nadir) by comparing measured reflectances to a lookup table of computed reflectances from a radiative transfer model (Remer et al., 2005). The reported uncertainties over ocean and non bright surfaces are $\pm 0.03 \pm 0.05\,\tau$ and $\pm 0.05 \pm 0.15\,\tau$, respectively, where τ is aerosol optical depth (AOD) or AOT (Remer

AMTD
6, 5577–5619, 2013

et al., 2005). Additionally, the MODIS Deep Blue Algorithm provides AOT values over deserts and other bright surfaces where the reported uncertainties are approximately 20–30 % (Hsu et al., 2006). The Multi-angle Imaging SpectroRadiometer (MISR) instrument onboard the Terra satellite measures upwelling shortwave radiance in four spectral channels (446, 558, 672, and 867 nm) with nine view angles and spatial resolutions of about 250 m to 1.1 km. To produce the MISR Level 2 product (MIL2SAE, F12, 22) with a spatial resolution of 17.6 km, top-of-atmosphere radiances from 16 × 16 pixel areas of 1.1 km resolution are analyzed (Diner et al., 1999). The multispectral and multiangle instrument retrieves accurate AOT values, even over bright deserts (Christopher and Wang, 2004; Kahn et al., 2005), with expected uncertainties of ±0.05 for AOT < 0.5 and ±10 % for AOT > 0.5 (Martonchik et al., 1998). We use the aerosol spatial distribution from MODIS and MISR to help verify the SEVIRI results that we have developed in this paper.

The CALIPSO satellite flies in formation with the "A-Train" constellation of satellites that also includes the Aqua-MODIS used in this study (Stephens et al., 2002). The Cloud-Aerosol Lidar with Orthogonal Polarization (CALIOP) onboard the CALIPSO satellite measures polarization-sensitive backscatter vertical profiles at 532 and 1064 nm during the day and night at a resolution of 333 m (Vaughan et al., 2004). The backscatter vertical profiles give information on the location of clouds and aerosols in the atmosphere as they are associated with higher backscatter values than the clear sky background. The color ratio (1064/532 nm total attenuated backscatter) and depolarization ratio (perpendicular/parallel channels at 532 nm) profiles are computed from the backscatter measurements which helps separate clouds from aerosols. After locating cloud and aerosol layers by using the Selective, Iterated Boundary Locator (SIBYL), CALIPSO produces a vertical feature mask (VFM) product (Level 2, Version 3.1) that shows the spatial distribution of clouds and aerosols in the atmosphere (Liu et al., 2010). We use the CALIPSO VFM product for verifying the SEVIRI algorithm.

A valuable validation data set used in this study is from the FAAM BAe146 research aircraft data that retrieves detailed volcanic ash measurements from the Leosphere

AMTD
6, 5577–5619, 2013

355 nm Lidar, the Passive Cavity Aerosol Spectrometer Probe (PCASP), and the Cloud and Aerosol Spectrometer (CAS) (Marenco et al., 2011). The FAAM BAe146 aircraft flew on six days in May 2010 where aerosol extinction and AOTs at 355 nm were retrieved along with ash mass concentrations and size distributions (Marenco et al., 2011). This study focuses on 16 May and 17 May since the volcanic ash was associated with higher AOTs on these days. We utilized the AOT measurements at 355 nm retrieved from the lidar which samples the atmosphere from 2 km above the surface to 300 m below the aircraft. Thus, the lidar AOTs exclude any boundary layer contribution, except for the 17 May case where boundary layer aerosols contribute less the 0.05 to the AOT. After integrating the AOT measurements over every minute, each retrieved AOT value corresponded to an along-track distance of 8–10 km. Note that AOT can still be derived in the presence of clouds by using the instruments onboard the BAe146 aircraft to detect and mask the cloud contaminated areas in the vertical column of air beneath the aircraft. The usefulness of BAe146 aircraft measurements has been shown in a number of papers where the aircraft measurements were analyzed along with satellite measurements (Johnson et al., 2012; Christopher et al., 2009; Naeger et al., 2013).

3 Methodology

There is a rich heritage of classification algorithms with the most common ones using the concept of spectral signatures where for example clouds "look different" based on spectral signatures in some wavelengths when compared to aerosols and land. A classic paper by Saunders and Kriebel (1988) used spectral and some spatial signatures to separate pixels into cloud-free, partly cloudy, or overcast scenes. Using spectral thresholds alone can cause uncertainties in image classification since there could be spectral overlap between and among classes. Thus, it is not possible to accurately separate various classes based on limited information from spectral signatures alone (Ackerman et al., 2008). Martins et al. (2002) used spatial (textural) measures to sep-

AMTD
6, 5577–5619, 2013

arate aerosols from clouds over oceans due to the mean and standard deviation for a group of aerosol pixels being different than clouds. Spatial measures are a form of texture identification where a group of aerosol pixels appear different than clouds due to several measures and one example being their homogeneity. Therefore, combining spectral and spatial information reduces the frequency of misclassifications within an image.

In this paper, we take this a step further by using temporal information along with spectral and spatial information as the high temporal resolution of geostationary satellite sensors permits the use of these tests, but only a handful of studies have actually used temporal tests (Calle et al., 2006; de Wildt et al., 2007). Calle et al. (2006) proposed a fire detection technique that utilized temporal information from the 3.9 µm SEVIRI channel and showed that false alarm rates were lower than when detecting fires without using any temporal information. Typically the temperature from the 3.9 µm channel does not encounter large variations with time, but Calle et al. (2006) found that large increases occur with the onset of fires which helps better detection of fires. Cloud detection can also be improved when using temporal information since the temporal variation of the reflectance and temperature of a pixel is usually greatly impacted by the presence of clouds. For example, when analyzing the reflectance of the 0.6 µm SEVIRI channel for a pixel over a period of time, the variation in the reflectance will be minimal in most clear sky cases but rather large for most cases where clouds are present since clouds are typically much more heterogeneous than the underlying land surface. Then, de Wildt et al. (2007) developed temporal tests using reflectance and temperature channels from SEVIRI and found that these tests helped mask clouds and cloud shadows which ultimately led to more accurate detection of snow cover. Although the temporal tests detected most clouds due to their heterogeneity, they had to rely on the spectral tests to detect the water clouds that were rather homogeneous since the reflectance and temperature channels showed little temporal variation. Another issue that often arises when using temporal techniques is the overestimation of cloud cover especially in areas near cloud edges and in areas over broken clouds where a pixel

AMTD
6, 5577–5619, 2013

may be cloud free in the current time-step but cloudy in the previous one. This situation can cause a significant increase in the variation of reflectance and temperature with time for a cloud free pixel. Therefore, even though temporal techniques have been used successfully for detecting fires and clouds, they also encounter problems that are investigated further in this study.

3.1 General flow of algorithm

For our algorithm, we first identify pixels that are land (or over land) and pixels that are water (or over water) to make the algorithm efficient and save computational time. This is necessary since the thresholds used to identify aerosols and clouds are different over water than over land. Classification methods are usually easier over water since water has a low visible reflectance and warmer infrared temperatures when compared to aerosols and clouds. However, over land spectral tests pose challenges since the surface reflectance and temperatures can be highly variable. After separating land and water pixels, we then identify cloudy pixels through a series of spectral threshold tests which are labeled as cloud and no longer processed by the algorithm. It is critical to identify cloud pixels because the final goal of this algorithm is to label all cloud-free aerosol pixels. All non-cloud pixels undergo further processing as we identify feature pixels through a series of threshold tests involving both spectral and temporal tests. Feature pixels are simply pixels that are contaminated with any type of aerosol or cloud. Finally, all pixels labeled as feature are fed into the final threshold tests that attempt to identify any remaining clouds through spectral, spatial, and temporal tests. If the feature pixel passes one of these tests, then it is labeled as cloud. If the pixel fails all of these tests, then the pixel is labeled as aerosol. Since the aerosol spatial distribution maps can be produced every 15 min when using SEVIRI, they can provide near real-time information on the location of volcanic ash which is a major aviation concern (Casadevall, 1992). Also, understanding the spatial distribution of aerosol and cloud is very important as this is the first step to accurately quantifying the cloud and aerosol radiative forcing (Kaufman et al., 2002).

AMTD
6, 5577–5619, 2013

3.2 Input data for algorithm

The US Geological Survey (USGS) global land cover characteristics database version 2.0, SEVIRI viewing and solar zenith angles, and the SEVIRI channels highlighted in Table 1 are input into our algorithm. SEVIRI viewing and solar zenith angles are primarily used for masking sun glint regions and for removing the solar component from the 3.9 µm channel while the SEVIRI channels provide the critical reflectivity and temperature values for each pixel. The USGS global land cover data is used immediately in the algorithm to separate land and water pixels and to find bright (e.g., desert) and non-bright (e.g., vegetation) pixels over land since certain threshold tests are not valid over bright surfaces with high reflectivity. Next, we develop a clear sky reflectance map by finding the minimum top of atmosphere (TOA) 0.6 µm reflectance for each pixel over a two-week period surrounding the time of interest (Jolivet et al., 2008). For example, if analyzing a 13:00 UTC SEVIRI image on 19 April 2010, then we find the minimum 0.6 µm reflectance from 12 April until 26 April at 13:00 UTC for each pixel which generates the clear sky reflectance map. For bright surfaces determined by the USGS global land cover map, we find the highest 10.8 µm temperature during the two week period and then extract the 0.6 µm reflectance from this particular pixel. Dust over desert regions can reduce the observed TOA reflectance below the actual clear-sky reflectance since dust is slightly absorbing at 0.6 µm (Patadia et al., 2009). While generating the minimum 0.6 µm reflectance maps, the standard deviation (σ) for the SEVIRI solar zenith angles (SZA) over the two-week period are computed for each pixel. The σSZA map is used along with the 0.6 µm clear sky reflectance map in an important threshold test which is discussed later in this section.

3.3 Initial cloud detection tests over land

After generating the σSZA and clear sky reflectance maps, the algorithm begins with the initial cloud detection tests shown in Table 2 which are all spectral tests. However, not shown in Table 2 is an ice and snow detection scheme that is applied over both

AMTD
6, 5577–5619, 2013

land and water pixels prior to the initial cloud detection tests so that these bright pixels can be ignored throughout the remainder of the algorithm. This ice and snow detection scheme uses the normalized difference snow index (NDSI), which takes advantage of snow being more reflective at 0.6 µm than at 1.6 µm (Riggs and Hall, 2004), along with other temporal tests. For all the temporal tests used in Table 2, the standard deviation (σ) of three successive 15 min SEVIRI images centered on the current image is computed for the highlighted channels in Table 1. Temporal tests help reduce the frequency of falsely detected clouds as snow or ice (Riggs and Hall, 2004), and for this study we use the σ of the 1.6 and 10.8 µm as the reflectance and temperature of snow and ice which typically vary slowly with time (de Wildt et al., 2007). However, we will not go any further into the specifics of the snow and ice detection scheme because it is not critical to the main goal of the algorithm and the results of this paper.

Spectral tests can separate cloud from aerosol and land surfaces due to the differing spectral signatures of these features. For example, Fig. 1 is a SEVIRI RGB image on 17 May 2010 at 13:30 UTC over Europe and the Atlantic Ocean where the four boxes indicate the location of extracted samples for ocean, ash, ice cloud, and water cloud. Figure 2a is a wavelength versus reflectivity plot for the three SEVIRI reflectivity channels showing the mean and one standard deviation for the extracted samples in Fig. 1 where the ocean is black, ash is blue, ice cloud is red, and water cloud is pink. Figure 2b is the same as Fig. 2a except wavelength versus temperature for four SEVIRI temperature channels is displayed. For the reflectivity channels, the water and ice clouds have much higher reflectivity than the ocean while the reflectivity of ash is only about 5–10 % higher than the ocean. Also, the trends across the reflectivity channels is important as the reflectivity increases or stays nearly constant for the water and ice cloud when moving from the 0.6 to 0.8 µm channels while the reflectivity decreases for the ash and ocean pixels. This difference in the trends for these features is due to the difference in particle sizes and imaginary refractive indices. The mean ash reflectivity is only about 5 % at 1.6 µm which is mostly due to the fact that the majority of ash particles are generally smaller than this channel wavelength (Weber et al., 2012). This also

AMTD
6, 5577–5619, 2013

explains the decreasing reflectivity trend for ash across these wavelengths. The much higher water cloud than ice cloud reflectivity at 1.6 µm is due to the higher imaginary refractive indices for ice which means the ice particles absorb more of the incoming radiation than water particles leading to lower TOA reflectivity. In Fig. 2b, the much larger temperature decrease from 3.9 to 8.7 µm for ice and water clouds compared to the ash and ocean is due to the added solar reflection component to the 3.9 µm channel. Water and ice particles reflect much of this incoming solar radiation back towards the satellite. The water cloud temperature decrease is larger than that for the ice cloud because the imaginary refractive index for ice is larger than water at 3.9 µm. When analyzing the temperature trend between the 10.8 and 12.0 µm channels, the temperature actually increases with wavelength for ash but decreases for the other features which is due to the unique characteristic of the ash imaginary refractive index being higher at 12.0 than at 10.8 µm causing the slightly lower temperatures at 12.0 µm (Ackerman, 1997). For the spectral threshold tests in Table 2 we used the differing spectral signatures of water, land, cloud, and aerosol to develop the algorithm.

The first initial cloud detection test is applied over only bright pixels where a high 0.6 µm reflectance threshold of 60 % is used to detect clouds which ensures that clear sky pixels are not falsely detected as clouds since the highest surface reflectance (i.e., non snow/ice) observed by this study was around 55 % over the Sahara Desert. The second cloud detection test in Table 2 is only applied over non-bright pixels and uses BTD 10.8–12.0 > −0.2 K in order to prevent the test from being applied over pixels contaminated with moderate to thick ash that can have reflectivity of 0.6 µm > 35 %. Thus, this test is developed primarily to detect clouds in regions of no ash or thin ash. The BTD 10.8-12.0 technique has been used extensively for both dust and volcanic ash detection as these particular aerosol types have been shown to be associated with negative values while clouds and pristine skies are typically associated with positive values (Brindley, 2007; Zhu et al., 2011; Zhang et al., 2006). Conversely, the purpose of the third cloud detection test is to detect clouds in regions of moderate to thick ash that causes negative BTD 10.8-12.0 while the presence of cloud causes the 0.6 µm re-

AMTD
6, 5577–5619, 2013

flectivity > 50 %. This study found that even the thickest ash regions will typically have 0.6 µm reflectivity < 50 % after observing that freshly emitted ash nearby the Eyjafjallajökull volcano had 0.6 µm reflectivity < 50 %. Also, note that the moderate ash plume over water in Fig. 1 where MODIS retrieved AOD is > 0.5 only has a 0.6 µm reflectivity of only about 12 %. The fourth initial cloud detection test is a very simple test that simply labels pixels with 10.8 µm < 240 K as ice cloud. This test can be confidently used in this study since pixels with 10.8 µm < 240 K are usually snow covered which our snow detection scheme has already found. Then, the fifth initial cloud detection test in Table 2 utilizes the BTD between 3.9 and 10.8 µm (BTD 3.9-10.8) which takes into account the SZA (θ) as the 3.9 µm channel is affected by solar radiation during the daytime (Christopher et al., 2012; Zhang et al., 2006).

Figure 3 shows bispectral plots for the SEVIRI channels of most interest to this study from the samples in Fig. 1 where ocean is black, ash is blue, ice cloud is red, and water cloud is pink. Figure 3b reveals that the thick ash over water is associated with BTD3.9-10.8 of about 3 K while the ice and water clouds are primarily associated with much larger values. Thus, we use a threshold of BTD 3.9-10.8 > 8 K for cloud detection which is able to detect the majority of clouds without misclassifying aerosols as clouds. The last initial cloud detection test uses the BTD between the 8.7 and 10.8 µm channels (BTD 8.7-10.8) along with BTD 10.8-12.0 which Zhang et al. (2006) has shown detects ice clouds quite accurately when using the 8.5, 11.0, and 12.0 µm channels of MODIS. Since the corresponding SEVIRI channels have slightly different central wavelengths and bandwidths than the MODIS channels, we found that the most appropriate BTD 8.7-10.8 threshold was −1 K instead of 0 K used in Zhang et al. (2006) as indicated in Fig. 3a where the ice clouds have BTD 8.7-10.8 from 0 to −2 K and BTD 10.8-12.0 from 2 to 3 K.

3.4 Feature detection tests over land

After the initial cloud detection tests, we apply feature detection tests to determine whether an atmospheric feature (i.e., cloud or aerosol) exists in a pixel. Note that these

AMTD
6, 5577–5619, 2013

feature detection tests only label a pixel as a feature temporarily until the final cloud detection tests in Table 2 separate the feature pixels as cloud or aerosol. The first feature detection test simply uses BTD 10.8-12.0 < −0.2 K to determine the pixel as a feature which detects most thick ash and dust regions. The thick ash in Fig. 1 is easily detected with this feature detection scheme as indicated by the BTD 10.8-12.0 ranging from −1 to −2 K in Fig. 3a. Then, we apply the BTD 3.9-10.8 test once again but set a much lower threshold of 2 K to detect atmospheric features such as cloud and aerosols. As seen in Fig. 3b, this feature test detects the ash, water cloud, and ice cloud which have BTD 3.9-10.8 > 2 K while the ocean pixels have BTD 3.9-10.8 < 0 K. The ash is mostly associated with BTD 3.9-10.8 just above 2 K while both cloud types have much higher values especially the water cloud with values near 20 K. Lastly, the 0.6 µm clear sky reflectance maps along with the σ SZA maps are used to determine whether a pixel is a feature. If the difference between the 0.6 µm reflectance for the current SEVIRI pixel and its clear sky reflectance is greater than the σSZA (i.e., 0.6 μm_{cur} – 0.6 μm_{clr} > σSZA in Table 2), then the pixel is classified as a feature. However, in order to reduce the noise in the final aerosol maps produced by this algorithm, a minimum σSZA value of 2° is set over land. The minimum σSZA is higher over land due to the greater variability of surface reflectance with decreasing or increasing SZA. The 0.6 μm_{cur} – 0.6 μm_{clr} test detects features well since in the presence of an atmospheric feature such as ash the 0.6 µm reflectance is typically higher than in clear sky conditions. Figure 3c shows that the 0.6 µm ash reflectance is 10 to 15 % which is significantly higher than the ocean background reflectance of less than 5 %. However, this is a relatively simple case over water where the clear sky ocean reflectance is very low. The methodology is not as successful over land, especially bright land surfaces, since the higher 0.6 µm clear sky reflectance over these surfaces can completely mask the cloud or aerosol signal. In fact, the presence of an absorbing ash or dust layer over a bright surface can actually reduce the 0.6 µm reflectance below the clear sky reflectance. To account for these scenarios the fourth and final feature detection test is applied only over bright surfaces and uses the absolute value of the 0.6 μm_{cur} – 0.6 μm_{clr} test.

AMTD
6, 5577–5619, 2013

3.5 Final cloud detection tests over land

The algorithm now separates the feature pixels as cloud or aerosol by using a series of cloud detection tests to label clouds. If a feature pixel is not labeled as cloud by the cloud detection tests, then the pixel is labeled as aerosol. The first several cloud detection tests use only spectral techniques so we do not discuss these much further since we want to focus on the temporal tests that have rarely been used in previous research. Also, the results of the algorithm are nearly identical when removing these spectral tests proving that the temporal tests are capable of detecting most of the cloud cover. The first spectral test is included in the algorithm to detect high ice clouds that are rather homogeneous while the second and third spectral tests are used primarily to detect low level clouds that are rather homogenous. Temporal tests can have difficulty detecting clouds that are fairly homogeneous since their reflectivity and temperature do not vary much in time.

The remainder of the final cloud detection tests in Table 2 are mostly tests involving temporal techniques. Figure 3e–f highlights the potential in using temporal tests for separating cloud and aerosol as the reflectance and temperature for the channels show greater variation in time for the water and ice clouds than for the ash which causes the larger σ for the clouds in the scatter plots. Both the ice and water cloud show about the same amount of separation from the ash in Fig. 3e while the ice cloud shows far more separation than the water cloud from the ash in Fig. 3f. This suggests that temporal tests using the reflectivity channels are about equally as good at detecting both ice and water clouds while temporal tests using the temperature channels are more capable of detecting ice clouds. In this study, the temporal tests take three successive 15 min SEVIRI scans and calculate the σ for each pixel which is referred to as a σT test throughout the remainder of the paper. We decided to use only 3 successive SEVIRI images to calculate σ because using more successive images increases the likelihood that both aerosol and cloud could be included in the σ computation for a pixel where aerosol and cloud reside nearby, and we want to limit these scenarios as much as

AMTD
6, 5577–5619, 2013

possible. Also, by using only 3 successive images, this algorithm can be used in time sensitive situations, such as volcanic ash plumes interfering with air traffic, that require real-time decision making. We use σT tests with the 0.6, 1.6, and 12.0 µm channels where the appropriate thresholds were chosen based on analyzing scatter plots as in Fig. 3e–f. The fourth and fifth cloud detection tests are mostly used for detecting cloud among thin to moderate dust or ash since they only check pixels with BTD 10.8–12.0 < −0.2 K. Thin to moderate dust and ash typically do not have σT 0.6 µm > 4 % as indicated in Fig. 3e where the ash pixels are less than 1 % as they are more homogeneous compared to clouds. The fifth cloud detection test is actually a spatial test (i.e., σs tests) where σ is computed over a 3 × 3 pixel region. If σs 12.0 µm > 2.5 K, then the center pixel of the 3 × 3 pixel group is classified as a cloud. The σs and σT tests work on the similar principles of cloud typically being more heterogeneous than aerosol except that the σs test operates in space instead of time. This is demonstrated in Fig. 3d where the ice cloud pixels are associated with much higher σs 12.0 µm values than shown for the ash pixels. Thus, the σs 12.0 µm test has the ability to detect ice clouds above thin to moderate ash or dust since the pixel region is more heterogeneous than a pixel region with only ash or dust present. The sixth cloud detection test is applied over only non-bright land surfaces and uses a threshold of σT 1.6 µm > 2 %. This test also checks whether the pixel has a BTD10.8-12.0 > −1 K and 0.6 µm > 25 %. By decreasing the BTD10.8-12.0 threshold to −1 K, this test may operate on pixels that contain moderate to thick aerosol while the 0.6 µm threshold helps prevent highly reflecting aerosols from being detected as cloud since aerosols rarely have 0.6 µm > 25 %. Thus, we use this temporal test primarily for clouds among thicker ash and dust regions where the presence of clouds typically leads to increases in σT 1.6 µm. Next, the seventh cloud detection tests is similar to the sixth as a σT 1.6 µm threshold of 2 is used again, but this test looks for feature pixels with BTD3.9-10.8 > −4 K and BTD10.8-12.0 > −0.2 K. The BTD3.9-10.8 test helps detect those thinner cloud features (Ackerman et al., 1998) that did not quite meet the 0.6 µm threshold of 25 % in the previous test. Then, the final two cloud detection tests use different σt 12.0 µm thresholds over non-bright and bright

AMTD
6, 5577–5619, 2013

land surfaces with thresholds of 1.2 and 2, respectively. We observed scenarios of dust over desert leading to σT 12.0 µm of nearly 2 which is the reason for the different values used over bright and non-bright land. Lastly, the feature pixels that fail all of the final cloud detection tests are labeled as aerosol.

3.6 Over water algorithm

We briefly discuss the simpler over water algorithm in Table 3. Due to the relative homogeneity of the water, spatial tests are critical to the water algorithm while temporal tests are ignored. The water algorithm begins with very similar spectral tests as used over land with the only noteworthy differences being the second and last initial cloud detection tests. The second test uses the 1.6 µm channel since the reflectivity of water at this wavelength is typically less than 1 % in pristine sky conditions which makes it a good channel to use for detecting clouds over water. The last initial cloud detection test is mainly for high ice cloud detection as these cold clouds typically have BTD 10.8-12.0 > 1 K and BTD 8.7-12.0 K > 1 K since the refractive indices of ice particles are significantly larger at 8.7 and 10.8 µm than at 12.0 µm. After applying the initial cloud detection tests, similar feature detection tests are also used over water, except for the 1.6–0.6 µm tests which is a very good test over water where the reflectivity usually decreases with wavelength during pristine skies. A cloud or aerosol layer over water can cause higher reflectivity at 1.6 µm compared to 0.6 µm with the exception of aerosol layers composed of small particles such as smoke. Note that we use a lower minimum σSZA threshold over water of 1° as opposed to 2° applied over land. The value can be lowered over water since 0.6 µm clear sky reflectance values for a certain pixel over a 14 day period has less variability over water than over land due to the homogeneity of the water surface. After applying the feature detection schemes over water, spatial tests are used on the feature pixels in order to identify whether or not the pixels are cloud contaminated. The spatial tests utilize the 0.6, 0.8, 1.6, and 12.0 µm channels where σ is computed over a 3 × 3 pixel region as was done for the 12.0 µm channel over land. The strict thresholds used for the spatial tests shown in Fig. 1 were decided

AMTD
6, 5577–5619, 2013

upon after analyzing case studies and producing scatter plots (e.g., Fig. 3) and spatial maps for each of the channels. Since optically thick aerosols can be associated with significant spatial variability over a 3 × 3 pixel region, we use slightly different spatial tests when the BTD10.8-12.0 < −0.2 K as these pixels usually contain thick dust or ash aerosols. However, we observed situations where low level water clouds were associated with BTD10.8-12.0 < −0.2 K over the eastern and northern Atlantic Ocean. We also observed pixels with BTD10.8-12.0 < −0.2 K where both cloud and moderate to thick aerosol were present. Thus, the spatial tests taking into account feature pixels with BTD10.8-12.0 < −0.2 K are important for these particular scenarios. The BTD3.9-10.8 test helps keep cloud-free thick aerosols from becoming classified as cloud since we observed scenarios where cloud free aerosol pixels were associated with BTD3.9-10.8 > 20 K mostly near their source region, such as freshly emitted ash from the Eyjafjallajökull volcano. Finally, after applying all the cloud detection tests to the feature pixels, the pixels that fail all the tests and remain as features are labeled as aerosol.

4 Results and discussion

4.1 19 April 2010 case

The proposed SEVIRI algorithm was tested against numerous volcanic ash and desert dust cases, but this paper only focuses on several volcanic ash cases during the April and May 2010 Eyjafjallajökull eruption. However, note that the SEVIRI algorithm also performed well for dust episodes during June 2007 when large concentrations of dust were transported from the Saharan desert over the eastern Atlantic Ocean. Figure 4a is a SEVIRI RGB image on 19 April 2010 at 13:00 UTC when a substantial amount of ash was being emitted from the Eyjafjallajökull volcano (Webley et al., 2012). Note that in Fig. 4a–e the CALIPSO transect is either shown in blue or black. The volcanic ash is identified in the SEVIRI RGB image by the pinkish colors south of Iceland. Figure 4b is a SEVIRI 0.6 µm visible image where the clouds appear white against a dark background

AMTD
6, 5577–5619, 2013

while the final results of the SEVIRI algorithm are in Fig. 4c with the pixels labeled as clear over water (blue), clear over land (green), cloud (gray), aerosol (pink/orange), and ice/snow (white). A pixel colored in pink means that the aerosol was identified as a feature by one of the spectral tests in Tables 2 or 3 (e.g., the BTD 10.8-12.0 or BTD 3.9-10.8 tests under the feature tests section in Table 2) and a pixel colored in orange means the aerosol was identified as a feature by the temporal tests. The optically thick, fresh volcanic ash near the source region influences BTD 10.8-12.0 < -0.2 K leading to the pink color of the pixels while the thinner, aged volcanic ash over Europe influences BTD 10.8-12.0 > -0.2 K and BTD 3.9-10.8 < 2 which means the 0.6 µm$_{cur}$ – 0.6 µm$_{clr}$ feature test identified the ash and labeled the pixels in orange. At the time of this case study, the volcano was already discharging ash for several days and this ash was transported westerly. Falcon flights on 19 April identified ash layers across Germany with a 1.7 km thick ash layer found over Leipzig, Germany (51.3° N, 12.4° E) (Schumann et al., 2011). The SEVIRI algorithm successfully labels these pixels around Leipzig, Germany as aerosols and they are nearly all colored orange. Therefore, the commonly used BTD 10.8-12.0 spectral test is unable to detect this moderate ash plume over land which shows the importance of the temporal test in identifying ash. In fact, Fig. 4d shows an example of the outcome of the SEVIRI algorithm if all the temporal tests in the feature and final cloud tests sections in Tables 2 and 3 were removed. The algorithm is now only capable of labeling a few scattered pixels as aerosol across Europe and nearly all the aerosols vanish over water except for the fresh volcanic aerosols south of Iceland. Even though the SEVIRI RGB shows a fairly broad area of ash emitting from the volcano, the SEVIRI algorithm in Fig. 4c does not classify the entire area as ash which is due to the cloud cover evident among the ash in the SEVIRI 0.6 µm visible image (Fig. 4b).

Figure 4e shows MODIS AOD results for the 19 April 2010 volcanic ash case at approximately 13:00 UTC where MODIS pixels with cloud fraction larger than 25 % are shown in gray. The MODIS AOD results show a very small area of AOD for the freshly emitted ash plume south of Iceland since most of these pixels are identified as having

AMTD
6, 5577–5619, 2013

cloud fraction larger than 25 %. The SEVIRI algorithm results in Fig. 4c show a slightly larger area of AOD with the ash plume. Figure 4f reveals two MISR overpasses across the region on this day where the eastward and westward overpasses occurred at approximately 11:15 and 12:50 UTC respectively. The MISR measures the freshly emitted ash region at about the same time as MODIS and SEVIRI, and the MISR AOD spatial distribution suggests that the SEVIRI algorithm properly detects the ash. Note that pixels identified as cloud contaminated by MISR are in gray. MISR detects a large area of AOD ~ 0.2 to the west of the main ash plume (~ 60° N, 22° W) that is mostly detected as cloud by the SEVIRI algorithm and MODIS. A close examination of Fig. 4a–b suggests that the MISR cloud detection scheme has limitations as clouds are clearly impacting this area. Further away from the source region across Europe, the MODIS and SEVIRI spatial distributions show some similarities, especially in the optically thicker ash areas in western Germany (~ 50° N, 7° E). However, MODIS detects significantly less aerosol pixels across central and especially eastern Germany where the Falcon aircraft observed aged volcanic ash on this day. For this particular case when MODIS AOD is > 0.2 over land, then the SEVIRI algorithm is successful in detecting the ash regions, but the algorithm may encounter some problems detecting ash regions with AOD < 0.2 as MODIS detects a fairly significant region of aerosols in eastern France that are not detected by SEVIRI. Figure 4g is the CALIPSO VFM that is shown along the transect in Fig. 4a–e where clouds are in blue and aerosols are in orange. If one looks closely at the CALIPSO VFM, some clouds are detected near the top of the aerosol layer from about 44 to 49° N and northward of 49° N is primarily cloudy. The SEVIRI algorithm labels an area of aerosol and cloud along this portion of the CALIPSO transect where MODIS detects all cloud which suggests that the proposed algorithm is performing well in this region. Near 49° N when CALIPSO begins detecting high level clouds over low level aerosols, the SEVIRI algorithm begins showing all clouds instead of the mix of clouds and aerosols southward of this point which further suggests that the algorithm is quite accurate in this region. North of about 51° N along the CALIPSO transect the SEVIRI algorithm classifies almost all cloud which agrees with the CALIPSO VFM.

AMTD
6, 5577–5619, 2013

4.2 16 and 17 May 2010 case

Figure 5a–f are similar to Fig. 4a–f except that the former pertain to the 17 May 2010 case study at 13:00 UTC where a significant area of volcanic ash resided over the North Sea around 56° N and 7° W (Turnbull et al., 2012). Most of ash plume was detected as a feature by the 0.6 μm_{cur} – 0.6 μm_{clr} test as indicated by the orange pixels while only the thicker regions of the ash were detected with the BTD 10.8-12.0 feature test. This is clearly seen when removing the temporal tests from the SEVIRI algorithm as before and comparing the results in Fig. 5c–d. In Fig. 5d where no temporal tests were used only a small area of ash is labeled over the North Sea which shows the benefit of introducing the temporal tests in the algorithm. Not surprisingly, the use of the temporal tests in the algorithm also leads to many more pixels labeled as cloud over both water and land. According to the SEVIRI RGB image in Fig. 5a, it appears that the proposed algorithm in Fig. 5c successfully disregards cloud contaminated areas within the ash plume region over the North Sea as clouds are shown off the coast of the Netherlands (~ 56° N, 5° E) and these same clouds are labeled as clouds by our algorithm. Unfortunately CALIPSO does not make an overpass across this ash plume, but we can still use MODIS and MISR AOT to help verify the SEVIRI algorithm. Figure 5e shows MODIS AOD results for this 17 May case where there is some agreement between the aerosol spatial distributions from MODIS and the SEVIRI algorithm. Both MODIS and SEVIRI detect the thicker regions of the ash plume that can be identified with the BTD 10.8-12.0 spectral test and both reveal aerosols over the western portions of the North Sea. However, SEVIRI detects a larger ash area over the central and eastern portions of the North Sea than shown for MODIS as MODIS classifies cloud contaminated areas within the ash plume that appear cloud-free in the SEVIRI RGB imagery. Over western France, MODIS detects thin ash with AOD < 0.2 while the SEVIRI algorithm fails to identify any ash in this same region. Again, this discrepancy suggests that the SEVIRI algorithm has some uncertainties in trying to detect optically thin aerosol over land. Figure 5f shows eastward and westward MISR overpasses occurring at approx-

AMTD
6, 5577–5619, 2013

imately 11:40 and 13:20 UTC, respectively, on 17 May. Unfortunately, MISR does not directly orbit the main ash plume area over the North Sea, but it can still help validate the SEVIRI algorithm. The eastward MISR overpass suggests that the SEVIRI algorithm performs fairly well in detecting ash as the aerosol spatial distributions are similar except the region around 60° N and 5° W where SEVIRI has clear skies while MISR has aerosol with AOD < 0.2. MISR also detects aerosol with AOD > 0.4 at 48° N and 7° W that is labeled as cloud by the SEVIRI algorithm, but we believe this difference is most likely attributed to the 80 minute time difference between the SEVIRI and MISR measurements as the cloud field became more developed in this region by 13:00 UTC. Furthermore, MISR barely detects any aerosol off the west coast of the UK (54° W, 5° W) while MODIS shows a substantial region of low AOD here. Similar to MISR, the SEVIRI algorithm detects minimal aerosol in this region which suggests that MODIS may be identifying aerosol in an aerosol-free region.

The FAAM BAe146 aircraft flights on 16 and 17 May are very helpful for verifying the proposed SEVIRI algorithm. Figure 6c is a SEVIRI RGB image on 16 May at 15:00 UTC with the intricate BAe146 aircraft flight track shown in white. The BAe146 aircraft took off in southeast England (52.1° N, 0.3° W) at approximately 12:55 UTC and landed in northwestern France (47.7° N, 2.1° W) at about 18:10 UTC. Figure 6a has 355 nm AOD from the BAe146 aircraft in red with the corresponding AOD scale on the right y-axis and SEVIRI BTD10.8-12.0 in black with its scale on the left y-axis. The dots along the black line indicate the results from the SEVIRI algorithm along the aircraft flight with green, blue, and red denoting clear, cloud, and aerosol, respectively. Figure 6b shows SEVIRI BTD10.8-12.0 again in black along with 0.6 µm reflectivity in blue with its scale on the y-axis from 0 to 50 %. A nearest pixel approach is used to collocate SEVIRI to the BAe146 aircraft in space while we find the closest SEVIRI overpass time to each point along the BAe146 aircraft track to collocate in time. Thus, 15 min SEVIRI scans beginning 11:30 UTC and ending 17:00 UTC were used to produce Fig. 6a–b even though only the 15:00 UTC SEVIRI RGB imagery is in Fig. 6c.

AMTD
6, 5577–5619, 2013

The aircraft flight began in cloudy conditions across southeastern England and then headed northwest into an ash plume with scattered clouds as shown by Fig. 6c where the ash is highlighted by the pinkish colors and clouds by the green and yellowish colors. Since clouds were the dominant feature in southern England, AOD was not reported but as the aircraft tracked northwestward the AOD jumped to about 0.2 until thick ash was measured at about 55° N and 4.3° W with an AOD of nearly 0.9. The SEVIRI algorithm accurately classifies clouds in southern England, but then classifies a mix of clear skies, clouds, and aerosols where the low AOD of 0.2 is measured which again suggests that the SEVIRI algorithm has uncertainties in detecting optically thin aerosol regions. However, Fig. 6b shows several significant increases in 0.6 µm reflectivity in the low AOD region which hints at cloud contamination. Furthermore, the aerosol extinction coefficient profiles from the BAe146 aircraft on 16 May shown in Marenco et al. (2011) reveal some low level clouds in the low AOD region which suggests the SEVIRI algorithm is classifying clouds properly in this region. When the AOD reaches nearly 0.9, the SEVIRI algorithm classifies nearly all aerosol pixels adequately except for a few pixels which are associated with 0.6 µm > 40 % indicating possible cloud contamination. The aerosol extinction coefficient profiles in Marenco et al. (2011) also indicate low level cloud contamination below the thick ash. Thus, according to the BAe146 aircraft data, the SEVIRI algorithm is accurate in labeling a few cloud pixels among the ash. Then, another region of low AOD is measured by the aircraft before flying over thicker ash around 55.2° N and 3.9° W with an AOD of about 0.7. The aerosol is almost entirely missed by the SEVIRI algorithm in this low AOD region as the algorithm classifies mostly clouds. The highly varying 0.6 µm reflectivity among the low AOD suggests that clouds are a dominant feature in this region. In Marenco et al. (2011), low level clouds are revealed all along this section of the BAe146 flight track further hinting at the accuracy of the SEVIRI algorithm. The algorithm classifies some aerosol pixels in the higher AOD region, but clouds are classified more frequently here as the 0.6 µm reflectivity has a significant increase near the minimum in BTD10.8-12.0 indicating the presence of clouds among the thick ash. Also, fairly thick lower level

AMTD
6, 5577–5619, 2013

clouds are shown along the aerosol extinction profiles in Marenco et al. (2011) with this thicker ash region. Next, the aircraft encounters very thin ash along its track as AOD drops to near zero values. As expected the SEVIRI algorithm fails to detect any of this ash and classifies mostly clear skies along this portion of the aircraft track. The aircraft flies over one more noteworthy ash region as AOD jumps to about 0.4 and then quickly drops to 0.2 at about 53.8° N and 2.2° W. The ash associated with the AOD of 0.4 is successfully detected by the algorithm which appears to be cloud-free from analyzing the 0.6 µm reflectivity and aerosol extinction profiles in Marenco et al. (2011). However, immediately as the AOD decreases clouds become an issue once again as the 0.6 µm reflectivity jumps to about 35 %.

The 17 May BAe146 aircraft flight is overlaid in white on the SEVIRI RGB image from 14:00 UTC on that same day in Fig. 7c. However, for this flight, the aircraft started in northwestern France at 11:26 UTC and landed in southeast England at 16:58 UTC. As seen in the RGB image, the aircraft encountered the main ash plume over the North Sea while scattered clouds impacted the flight over England and Scotland. Figure 7a–b are the same as Fig. 6a–b except the aircraft AOD and SEVIRI measurements from 17 May are shown. The times when the aircraft were above the scattered clouds over land are clearly seen in Fig. 7b by the very significant increases in 0.6 µm reflectivity, and the SEVIRI algorithm successfully classifies these regions as cloud. After the first period of scattered clouds over land, the aircraft flies over ocean (~ 53° N, 2.5° W) before making a west to east path over land. When the aircraft is over the ocean, the SEVIRI algorithm classifies mostly clear skies with a mix of some cloud and aerosol. At this time, 355 nm AOD from the aircraft is very low with most values being less than 0.1 which suggests the SEVIRI algorithm has difficulty detecting aerosol over water when the AOD is > 0.1. The aircraft measures AOD near 0.2 during its brief west-east transect over land, but the SEVIRI algorithm classifies cloud in this region, and the algorithm appears to be correct according to the strong peak in 0.6 µm reflectivity and the BAe146 aerosol extinction profiles along this section of the aircraft track in Marenco et al. (2011). After traversing land, the aircraft immediately encounters the

AMTD
6, 5577–5619, 2013

main ash plume when flying over the North Sea as indicated by the large increase in 355 nm AOD to about 0.6 in Fig. 7a. However, the aircraft then descends beneath the ash plume which is why the AOD drops to zero while the SEVIRI algorithm detects aerosols. When the aircraft ascends, it measures the ash plume again as the AOD increases to nearly 0.4 before descending and measuring zero AOD the remainder of its flight path. From analyzing the SEVIRI 0.6 µm reflectivity along with the SEVIRI RGB image, it appears that cloud contamination is very minimal across the main ash plume region. Thus, the algorithm performs very well over the ash plume region as only one cloud pixel is detected amongst the aerosol pixels.

5 Conclusions

In this study we have developed a unique algorithm combining spectral, spatial, and temporal threshold tests using SEVIRI measurements to separate between clear skies, clouds, and aerosols. The algorithm is capable of detecting both dust and ash, but for this paper we only focus on the Eyjafjallajökull volcanic eruption period during April and May 2010 where substantial ash was transported from the volcano to over the North Sea and Europe. Aerosol (e.g., ash) spatial distribution maps were generated every hour during the daytime beginning with the initial eruption on 14 April and ending on 23 May. In this paper we focus specifically on the daytime volcanic ash cases on 19 April, 16 May, and 17 May when numerous sources of validation data were available. By using MODIS, MISR, CALIPSO, and BAe146 aircraft data as verification data, we show that the algorithm is capable of generating accurate aerosol spatial distribution maps even at these high latitudes. First, the SEVIRI aerosol spatial distribution maps show important similarities to the MODIS and MISR AOD products which suggests that the proposed algorithm works well. Second, the CALIPSO VFM suggests the SEVIRI algorithm can successfully distinguish between cloud and aerosol in complex cloud and aerosol regions over land. Lastly, the BAe146 aircraft shows that the SEVIRI algorithm detects nearly all ash regions over both land and water when AOD > 0.2. However, the

AMTD
6, 5577–5619, 2013

MODIS, MISR, and BAe146 aircraft data suggests that the algorithm may encounter some problems detecting ash when AOD < 0.1 over water and AOD < 0.2 over land.

Since the damaging effects of volcanic ash to commercial airplanes can be life threatening, accurately tracking ash during volcanic eruption periods is vital. Polar orbiting satellite sensors do not have the temporal resolution to effectively track volcanic ash. Thus, geostationary sensors, such as SEVIRI, are absolutely critical for tracking volcanic ash and ensuring the safety of people onboard commercial airplanes. The accurate aerosol spatial distribution maps which can be generated every 15 min by the proposed SEVIRI algorithm can serve as an extremely important tool during volcanic eruptions.

Acknowledgements. This research is sponsored by NASA's CALIPSO, Radiation Sciences, and ACMAP programs. Special thanks to Jim Haywood, Ben Johnson, and Franco Marenco for the aircraft data used in this paper.

References

Ackerman, S. A.: Remote sensing aerosols using satellite infrared observations, J. Geophys. Res., 102, 17069–17079, doi:10.1029/96jd03066, 1997.

Ackerman, S. A., Strabala, K. I., Menzel, W. P., Frey, R. A., Moeller, C. C., and Gumley, L. E.: Discriminating clear sky from clouds with MODIS, J. Geophys. Res., 103, 32141–32157, doi:10.1029/1998jd200032, 1998.

Ackerman, S. A., Holz, R. E., Frey, R., Eloranta, E. W., Maddux, B. C., and McGill, M.: Cloud detection with MODIS. Part II: Validation, J. Atmos. Ocean. Tech., 25, 1073–1086, 2008.

Ansmann, A., Tesche, M., Groß, S., Freudenthaler, V., Seifert, P., Hiebsch, A., Schmidt, J., Wandinger, U., Mattis, I., Müller, D., and Wiegner, M.: The 16 April 2010 major volcanic ash plume over central Europe: EARLINET lidar and AERONET photometer observations at Leipzig and Munich, Germany, Geophys. Res. Lett., 37, L13810, doi:10.1029/2010GL043809, 2010.

Ansmann, A., Tesche, M., Seifert, P., Groß, S., Freudenthaler, V., Apituley, A., Wilson, K. M., Serikov, I., Linné, H., Heinold, B., Hiebsch, A., Schnell, F., Schmidt, J., Mattis, I., Wandinger, U., and Wiegner, M.: Ash and fine-mode particle mass profiles from EARLINET-AERONET

AMTD
6, 5577–5619, 2013

observations over central Europe after the eruptions of the Eyjafjallajökull volcano in 2010, J. Geophys. Res.-Atmos., 116, D00U02, doi:10.1029/2010JD015567, 2011.
Brindley, H. E.: Estimating the top-of-atmosphere longwave radiative forcing due to Saharan dust from satellite observations over a west African surface site, Atmos. Sci. Lett., 8, 74–79, 2007.
Calle, A., Casanova, J. L., and Romo, A.: Fire detection and monitoring using MSG Spinning Enhanced Visible and Infrared Imager (SEVIRI) data, J. Geophys. Res.-Biogeo., 111, G04S06, doi:10.1029/2005JG000116, 2006.
Casadevall, T. J.: Volcanic hazards and aviation safety, Lessons from the past decade, Flight Safety Foundation – Flight Safety Digest, 1–9 May 1993, 210–220, 1992.
Christopher, S. A. and Wang, J.: Intercomparison between multi-angle imaging spectroradiometer (MISR) and sunphotometer aerosol optical thickness in dust source regions over China: implications for satellite aerosol retrievals and radiative forcing calculations, Tellus B, 56, 451–456, 2004.
Christopher, S. A., Johnson, B., Jones, T. A., and Haywood, J.: Vertical and spatial distribution of dust from aircraft and satellite measurements during the GERBILS field campaign, Geophys. Res. Lett., 36, L06806, doi:10.1029/2008gl037033, 2009.
Christopher, S. A., Feng, N., Naeger, A. R., Johnson, B. T. T., and Marenco, F.: Satellite Remote Sensing Analysis of the 2010 Eyjafjallajökull Volcanic Ash Cloud over the North Sea during May 4–May 8, 2010, J. Geophys. Res., 117, D00U20, doi:10.1029/2011JD016850, 2012.
de Ruyter de Wildt, M., Seiz, G., and Gruen, A.: Operational snow mapping using multitemporal Meteosat SEVIRI imagery, Remote Sens. Environ., 109, 29–41, 2007.
Diner, D. J., Abdou, W. A., Ackerman, T. P., Crean, K., Gordon, H. R., Kahn, R. A., Martonchik, J. V., McMuldrock, S., Paradise, S. R., Pinty, B., Verstraete, M. M., Wang, M., and West, R.: Level 2 Aerosol Retrieval Algorithm Theoretical Basis, Rep. D11400, Rev. D, Jet Propulsion Laboratory, Pasadena, California, 1999.
Hsu, N. C., Si-Chee, T., King, M. D., and Herman, J. R.: Deep Blue Retrievals of Asian Aerosol Properties During ACE-Asia, IEEE T. Geosci. Remote, 44, 3180–3195, 2006.
Johnson, B., Turnbull, K., Brown, P., Burgess, R., Dorsey, J., Baran, A. J., Webster, H., Haywood, J., Cotton, R., Ulanowski, Z., Hesse, E., Woolley, A., and Rosenberg, P.: In situ observations of volcanic ash clouds from the FAAM aircraft during the eruption of Eyjafjallajökull in 2010, J. Geophys. Res., 117, D00U24, doi:10.1029/2011JD016760, 2012.

AMTD
6, 5577–5619, 2013

Jolivet, D., Ramon, D., Bernard, E., Deschamps, P.-Y., Riedi, J., Nicolas, J.-M., and Hagolle, O.: Aerosol monitoring over land using MSG/SEVIRI, EUMETSAT Meteorological Satellite Conference, 8–12 September 2008, Darmstadt, Germany, 2008.

Kahn, R. A., Gaitley, B. J., Martonchik, J. V., Diner, D. J., Crean, K. A., and Holben, B.: Multiangle Imaging Spectroradiometer (MISR) global aerosol optical depth validation based on 2 years of coincident Aerosol Robotic Network (AERONET) observations, J. Geophys. Res., 110, D10S04, doi:10.1029/2004jd004706, 2005.

Kaufman, Y. J., Tanre, D., and Boucher, O.: A satellite view of aerosols in the climate system, Nature, 419, 215–223, 2002.

Krotkov, N. A., Torres, O., Seftor, C., Krueger, A. J., Kostinski, A., Rose, W., Bluth, G., Schneider, D., and Schaefer, S.: Comparison of TOMS and AVHRR volcanic ash retrievals from the August 1992 eruption of Mt. Spurr, Geophys. Res. Lett., 26, 455–458, 1999.

Liu, Z., Kuehn, R., Vaughan, M., Winker, D., Omar, A., Powell, K., Trepte, C., Hu, Y., and Hostetler, C. : The CALIPSO Cloud And Aerosol Discrimination: Version 3 Algorithm and Test Results, 25th International Laser Radar Conference (ILRC), 5–9 July 2010, St. Petersburg, Russia, 2010.

Marenco, F., Johnson, B., Turnbull, K., Newman, S., Haywood, J., Webster, H., and Ricketts, H.: Airborne lidar observations of the 2010 Eyjafjallajkull volcanic ash plume, J. Geophys. Res., 116, D00U05, doi:10.1029/2011JD016396, 2011.

Martins, J. V., Tanré, D., Remer, L., Kaufman, Y., Mattoo, S., and Levy, R.: MODIS cloud screening for remote sensing of aerosols over oceans using spatial variability, Geophys. Res. Lett., 29, 4-1–4-4, 2002.

Martonchik, J. V., Diner, D. J., Kahn, R. A., Ackerman, T. P., Verstraete, M. M., Pinty, B., and Gordon, H. R.: Techniques for the retrieval of aerosol properties over land and ocean using multiangle imaging, IEEE T. Geosci. Remote, 36, 1212–1227, 1998.

Mason, B. G., Pyle, D. M., and Oppenheimer, C.: The size and frequency of the largest explosive eruptions on Earth, Bull. Volcanol., 66, 735–748, 2004.

Mastin, L. G., Guffanti, M., Servranckx, R., Webley, P., Barsotti, S., Dean, K., Durant, A., Ewert, J. W., Neri, A., Rose, W. I., Schneider, D., Siebert, L., Stunder, B., Swanson, G., Tupper, A., Volentik, A., and Waythomas, C. F.: A multidisciplinary effort to assign realistic source parameters to models of volcanic ash-cloud transport and dispersion during eruptions, J. Volcanol. Geoth. Res., 186, 10–21, 2009.

AMTD
6, 5577–5619, 2013

Millington, S. C., Saunders, R. W., Francis, P. N., and Webster, H. N.: Simulated volcanic ash imagery: A method to compare NAME ash concentration forecasts with SEVIRI imagery for the Eyjafjallajkull eruption in 2010, J. Geophys. Res., 117, D00U17, doi:10.1029/2011JD016770, 2012.

Naeger, A. R., Christopher, S. A., Ferrare, R., and Liu, Z.: A new technique using infrared satellite measurements to improve the accuracy of the CALIPSO cloud-aerosol discrimination method, IEEE T. Geosci. Remote, 51, 642–653, 2013.

Patadia, F., Yang, E.-S., and Christopher, S. A.: Does dust change the clear sky top of atmosphere shortwave flux over high surface reflectance regions?, Geophys. Res. Lett., 36, L15825, doi:10.1029/2009gl039092, 2009.

Pavolonis, M. J., Feltz, W. F., Heidinger, A. K., and Gallina, G. M.: A daytime complement to the reverse absorption technique for improved automated detection of volcanic ash, J. Atmos. Ocean. Tech., 23, 1422–1444, 2006.

Pergola, N., Tramutoli, V., Marchese, F., Scaffidi, I., and Lacava, T.: Improving volcanic ash cloud detection by a robust satellite technique, Remote Sens. Environ., 90, 1–22, 2004.

Prata, A. J.: Infrared radiative transfer calculations for volcanic ash clouds, Geophys. Res. Lett., 16, 1293–1296, 1989.

Prata, A. J. and Kerkmann, J.: Simultaneous retrieval of volcanic ash and SO2 using MSG-SEVIRI measurements, Geophys. Res. Lett., 34, L05813, doi:10.1029/2006GL028691, 2007.

Prata, F., Bluth, G., Rose, B., Schneider, D., and Tupper, A.: Comments on "Failures in detecting volcanic ash from a satellite-based technique", Remote Sens. Environ., 78, 341–346, 2001.

Remer, L. A., Kaufman, Y. J., Tanré, D., Mattoo, S., Chu, D. A., Martins, J. V., Li, R.-R., Ichoku, C., Levy, R. C., Kleidman, R. G., Eck, T. F., Vermote, E., and Holben, B. N.: The MODIS Aerosol Algorithm, Products, and Validation, J. Atmos. Sci., 62, 947–973, doi:10.1175/JAS3385.1, 2005.

Riggs, G. A. and Hall, D. K.: Snow Mapping with the MODIS Aqua Instrument, 61st Eastern Snow Conference, 9–11 June 2004, Portland, Maine, 81–84, 2004.

Saunders, R. W., and Kriebel, K. T.: An improved method for detecting clear sky and cloudy radiances from AVHRR data (North Atlantic), Int. J. Remote Sens., 9, 123–150, 1988.

Savtchenko, A., Ouzounov, D., Ahmad, S., Acker, J., Leptoukh, G., Koziana, I., and Nickless, D.: Terra and Aqua MODIS products available from NASA GES DAAC, Adv. Space Res., 34, 710–714, 2004.

AMTD
6, 5577–5619, 2013

Schmetz, J., Pili, P., Tjemkes, S., Just, D., Kerkmann, J., Rota, S., and Ratier, A.: An Introduction to Meteosat Second Generation (MSG), B. Am. Meteorol. Soc., 83, 977–992, doi:10.1175/1520-0477(2002)083<0977:AITMSG>2.3.CO;2, 2002.

Schumann, U., Weinzierl, B., Reitebuch, O., Schlager, H., Minikin, A., Forster, C., Baumann, R., Sailer, T., Graf, K., Mannstein, H., Voigt, C., Rahm, S., Simmet, R., Scheibe, M., Lichtenstern, M., Stock, P., Rüba, H., Schäuble, D., Tafferner, A., Rautenhaus, M., Gerz, T., Ziereis, H., Krautstrunk, M., Mallaun, C., Gayet, J.-F., Lieke, K., Kandler, K., Ebert, M., Weinbruch, S., Stohl, A., Gasteiger, J., Groß, S., Freudenthaler, V., Wiegner, M., Ansmann, A., Tesche, M., Olafsson, H., and Sturm, K.: Airborne observations of the Eyjafjalla volcano ash cloud over Europe during air space closure in April and May 2010, Atmos. Chem. Phys., 11, 2245–2279, doi:10.5194/acp-11-2245-2011, 2011.

Sigmundsson, F., Hreinsdóttir, S., Hooper, A., Árnadóttir, T., Pedersen, R., Roberts, M. J., Óskarsson, N., Auriac, A., Decriem, J., Einarsson, P., Geirsson, H., Hensch, M., Ófeigsson, B. G., Sturkell, E., Sveinbjörnsson, H., and Feigl, K. L.: Intrusion triggering of the 2010 Eyjafjallajökull explosive eruption, Nature, 468, 426–432, 2010.

Stephens, G. L., Vane, D. G., Boain, R. J., Mace, G. G., Sassen, K., Wang, Z., Illingworth, A. J., O'Connor, E. J., Rossow, W. B., Durden, S. L., Miller, S. D., Austin, R. T., Benedetti, A., Mitrescu, C., and CloudSat Science Team, T.: THE CLOUDSAT MISSION AND THE A-TRAIN: A new dimension to space-based observations of clouds and precipitation, B. Am. Meteorol. Soc., 83, 1771–1790, doi:10.1175/BAMS-83-12-1771, 2002.

Torres, O., Bhartia, P. K., Herman, J. R., Ahmad, Z., and Gleason, J.: Derivation of aerosol properties from satellite measurements of backscattered ultraviolet radiation: Theoretical basis, J. Geophys. Res., 103, 17099–17110, 1998.

Turnbull, K., Johnson, B., Marenco, F., Haywood, J., Minikin, A., Weinzierl, B., Schlager, H., Schumann, U., Leadbetter, S., and Woolley, A.: A case study of observations of volcanic ash from the Eyjafjallajökull eruption: 1. in situ airborne observations, J. Geophys. Res., 117, D00U12, doi:10.1029/2011JD016688, 2012.

Vaughan, M. A., Young, S. A., Winker, D. M., Powell, K. A., Omar, A. H., Liu, Z., Hu, Y., and Hostetler, C. A.: Fully automated analysis of space-based lidar data: an overview of the CALIPSO retrieval algorithms and data products, Maspalomas, Gran Canaria, Spain, 16–30, 2004.

Weber, K., Eliasson, J., Vogel, A., Fischer, C., Pohl, T., van Haren, G., Meier, M., Grobéty, B., and Dahmann, D.: Airborne in-situ investigations of the Eyjafjallajökull volcanic ash plume

AMTD
6, 5577–5619, 2013

on iceland and over north-western Germany with light aircrafts and optical particle counters, Atmos. Environ., 48, 9–21, 2012.
Webley, P. W., Steensen, T., Stuefer, M., Grell, G., Freitas, S., and Pavolonis, M.: Analyzing the Eyjafjallajkull 2010 eruption using satellite remote sensing, lidar and WRF-Chem dispersion and tracking model, J. Geophys. Res., 117, D00U26, doi:10.1029/2011JD016817, 2012.
Zhang, P., Lu, N. N., Hu, X. Q., and Dong, C. H.: Identification and physical retrieval of dust storm using three MODIS thermal IR channels, Global Planet. Change, 52, 197–206, 2006.
Zhu, L., Liu, J., Liu, C., and Wang, M.: Satellite remote sensing of volcanic ash cloud in complicated meteorological conditions, Sci. China Earth Sci., 54, 1789–1795, 2011.

AMTD
6, 5577–5619, 2013

Table 1. SEVIRI channels with the center, minimum, and maximum wavelengths where the channels used in the SEVIRI algorithm are highlighted in bold.

Channel	Center (μm)	Min (μm)	Max (μm)
1	**0.635**	**0.56**	**0.71**
2	**0.81**	**0.74**	**0.88**
3	**1.64**	**1.5**	**1.78**
4	**3.9**	**3.48**	**4.36**
5	6.25	5.35	7.15
6	7.35	6.85	7.85
7	**8.7**	**8.3**	**9.1**
8	9.66	9.38	9.94
9	**10.8**	**9.8**	**11.8**
10	**12**	**11**	**13**
11	13.4	12.4	14.4

AMTD
6, 5577–5619, 2013

Table 2. Outline of the algorithm applied over land which shows the various thresholds used for the initial cloud tests, feature tests, and final cloud tests and the scene restrictions for each test.

Tests	Scenes
Initial cloud tests	
0.6 µm > 60 %	Bright pixels only
0.6 µm > 35 % and BTD 10.8–12.0 > −0.2 K	Non bright pixels only
0.6 µm > 50 % and BTD 10.8–12.0 < −0.2 K	Non bright pixels only
10.8 µm < 240 K	All pixels
BTD 3.9–10.8 > 8 K and BTD 10.8–12.0 > −0.2 K	All pixels
BTD 8.7–10.8 > −1 K and BTD 10.8–12.0 > 0 K	All pixels
Feature tests	
BTD 10.8–12.0 < −0.2 K	All non cloud pixels
BTD 3.9–10.8 > 2 K	All non cloud pixels
$0.6\,\mu m_{CUR} - 0.6\,\mu m_{CLR} > \sigma SZA$	Non cloud and non bright pixels only
$\lvert 0.6\,\mu m_{CUR} - 0.6\,\mu m_{CLR} \rvert > \sigma SZA$	Non cloud and bright pixels only
Final cloud tests	
BTD 3.9–10.8 > 2 K and BTD 8.7–10.8 > 1 K and BTD 10.8–12.0 > 1.0 K	All feature pixels
0.6 µm > 35 % and BTD 10.8–12.0 > −1.0 K	Non bright and feature pixels only
1.6 µm > 35 % and BTD 10.8–12.0 > 0 K	Non bright and feature pixels only
σT 0.6 µm > 4 % and BTD 10.8–12.0 < −0.2 K	All feature pixels
σs 12.0 µm > 2.5 K and BTD 10.8–12.0 < −0.2 K	All feature pixels
σT 1.6 µm > 2 % and BTD 10.8–12.0 > −1 K and 0.6 µm > 25 %	Non bright and feature pixels only
σT 1.6 µm > 2 % and BTD 10.8–12.0 > −0.2 K and BTD 3.9–10.8 > −4 K	Non bright and feature pixels only
σT 12.0 µm > 1.2 K and BTD 10.8–12.0 > −0.2 K	Non bright and feature pixels only
σT 12.0 µm > 2 K and BTD 10.8–12.0 > −0.2 K	Bright and feature pixels only

AMTD
6, 5577–5619, 2013

Table 3. Outline of the algorithm applied over water which shows the various thresholds used for the initial cloud tests, feature tests, and final cloud tests and the scene restrictions for each test.

Tests	Scenes
Initial cloud tests	
0.6 µm > 35 % and BTD 10.8–12.0 > −0.2 K	All pixels
1.6 µm > 35 % and BTD 10.8–12.0 > −0.2 K	All pixels
0.6 µm > 50 % and BTD 10.8–12.0 < −0.2 K	All pixels
10.8 µm < 240 K	All pixels
BTD 3.9–10.8 > 8 K and BTD 10.8–12.0 > 0 K	All pixels
BTD 8.7–10.8 > −1 K and BTD 10.8–12.0 > 0 K	All pixels
BTD 8.7–12.0 > 1 K and BTD 10.8–12.0 > 1 K	All pixels
Feature tests	
BTD 10.8–12.0 < −0.2 K	All non cloud pixels
1.6 µm − 0.6 µm > 1 %	All non cloud pixels
$0.6\,\mu m_{CUR} - 0.6\,\mu m_{CLR} > \sigma SZA$	All non cloud pixels
Final cloud tests	
σs 12.0 µm > 2.5 K and BTD 10.8–12.0 > −0.2 K	All feature pixels
σs 1.6 µm > 2.5 % and BTD 10.8–12.0 > −0.2 K	All feature pixels
σs 12.0 µm > 1 K and BTD 10.8–12.0 < −0.2 K and BTD 3.9–10.8 < 20 K	All feature pixels
σs 0.6 µm > 3 % and BTD 10.8–12.0 < −0.2 K and BTD 3.9–10.8 < 20 K	All feature pixels
σs 0.8 µm > 2 % and $m s$ 0.8 > 30 %	All feature pixels
1.6 µm > 25 % and BTD 8.7–10.8 < −3 K and BTD 10.8–12.0 < 0 K	All feature pixels

AMTD
6, 5577–5619, 2013

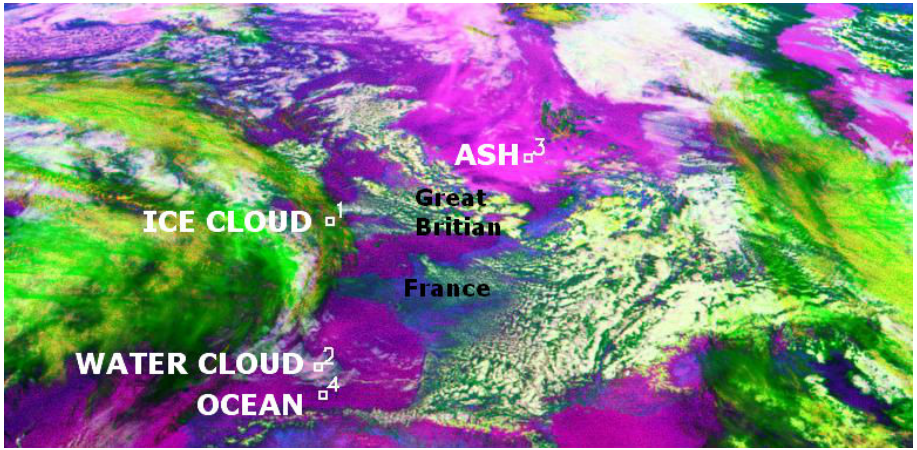

Fig. 1. SEVIRI RGB image on 17 May 2010 at 13:30 UTC over Europe and the Atlantic Ocean where the four boxes indicate the location of extracted samples for ocean, ash, ice cloud, and water cloud.

AMTD
6, 5577–5619, 2013

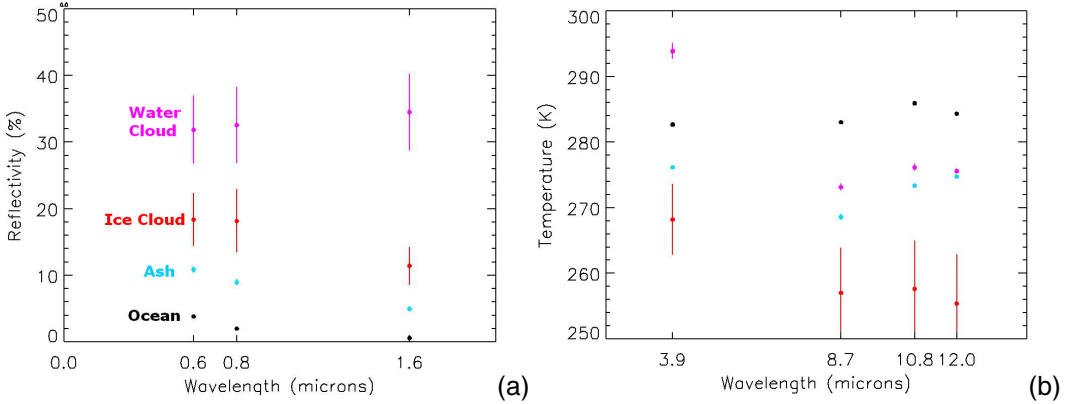

Fig. 2.
(a) Wavelength versus reflectivity plot for the three SEVIRI reflectivity channels showing the mean and one standard deviation for the extracted samples in Fig. 2 where the ocean is black, ash is blue, ice cloud is red, and water cloud is pink. **(b)** Same as **(a)** except wavelength versus temperature for four SEVIRI temperature channels.

AMTD
6, 5577–5619, 2013

The identification of volcanic ash using the MSG SEVIRI

A. R. Naeger and
S. A. Christopher

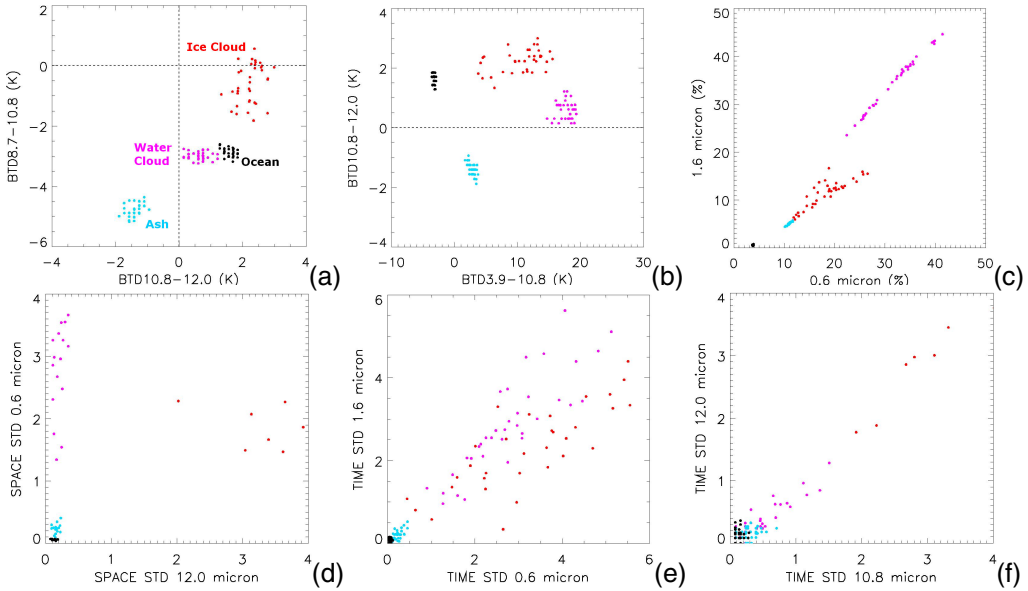

Fig. 3.
Bispectral plots for the SEVIRI channels of most interest to this study from the samples in Fig. 2 where ocean is black, ash is blue, ice cloud is red, and water cloud is pink. **(a)** BTD10.8-12.0 versus BTD8.7-10.8, **(b)** BTD3.9-10.8 versus BTD10.8-12.0, **(c)** 0.6 µm versus 1.6 µm, **(d)** σs 12.0 µm versus σs 0.6 µm, **(e)** σT 0.6 µm versus σT 1.6 µm, and **(f)** σT 10.8 µm versus σT 12.0 µm.

AMTD
6, 5577–5619, 2013

The identification of volcanic ash using the MSG SEVIRI

A. R. Naeger and
S. A. Christopher

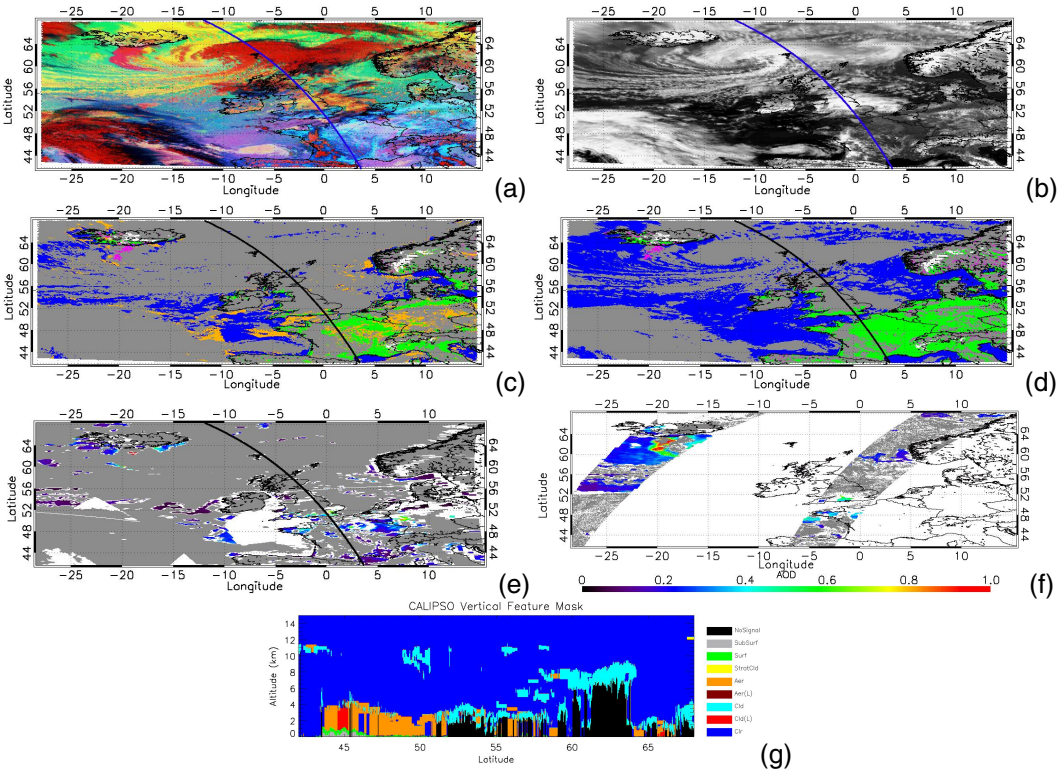

Fig. 4.
Caption on next page.

AMTD
6, 5577–5619, 2013

The identification of volcanic ash using the MSG SEVIRI

A. R. Naeger and
S. A. Christopher

Fig. 4. (a) SEVIRI RGB image on 19 April 2010 at 13:00 UTC when a substantial amount of ash was being emitted from the Eyjafjallajökull volcano. The volcanic ash is identified in the SEVIRI RGB image by the pinkish colors south of Iceland. **(b)** SEVIRI Ch1 visible image where clouds appear white against a dark background. **(c)** Final results of the SEVIRI algorithm with the pixels labeled as clear over water (blue), clear over land (green), cloud (gray), aerosol (pink/orange), and ice/snow (white). A pixel colored in pink means that the aerosol was identified as a feature by one of the spectral tests in Tables 2 or 3 (e.g. the BTD 10.8-12.0 or BTD 3.9-10.8 tests under the feature tests section in Table 2) and a pixel colored in orange means the aerosol was identified as a feature by the temporal tests. **(d)** Same as **(c)** except results are shown if all the temporal tests in the feature and final cloud tests sections in Tables 2 and 3 were removed. **(e)** MODIS AOD results for 19 April at approximately 13:00 UTC where MODIS pixels with cloud fraction larger than 25 % are shown in gray. **(f)** MISR AOD across the region on this day where the eastward and westward overpasses occurred at approximately 11:15 and 12:50 UTC respectively. Pixels identified as cloud contaminated by MISR are in gray. **(g)** CALIPSO VFM that is shown along the transect in **(a)**–**(e)** where clouds are in blue and aerosols are in orange. Note that CALIPSO transects are denoted by the black or blue lines in **(a)**–**(e)**.

AMTD
6, 5577–5619, 2013

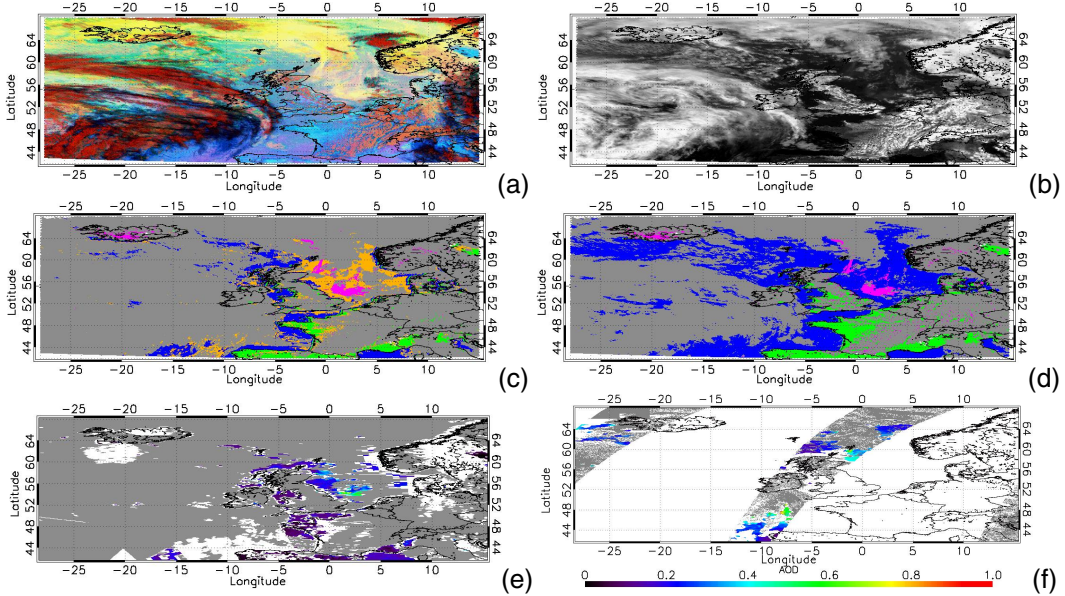

Fig. 5.
(a)–(d) are same as in Fig. 4 except that this is a SEVIRI RGB image on 17 May 2010 at 13:00 UTC where a significant area of volcanic ash resided over the North Sea around 56° N and 7° W. **(e)** MODIS AOD results for the 17 May case from 13:10 to 13:30 UTC. **(f)** MISR AOD results for the eastward and westward overpasses occurring at approximately 11:40 and 13:20 UTC, respectively, on 17 May.

AMTD
6, 5577–5619, 2013

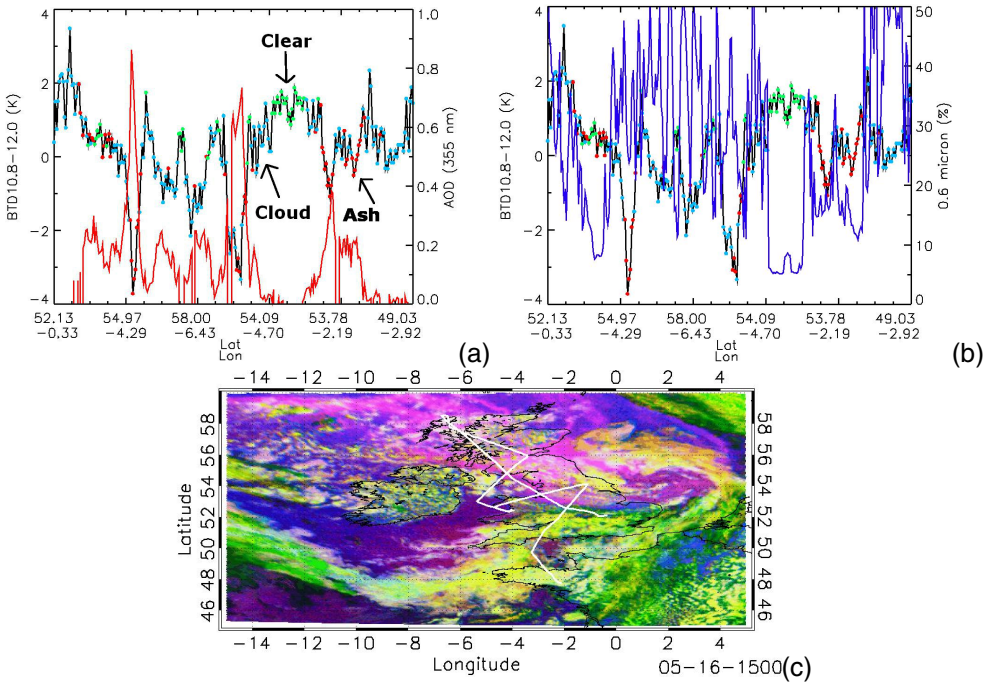

Fig. 6.
(a) 355 nm AOD from the BAe146 aircraft in red with the corresponding AOD scale on the right y-axis and SEVIRI BTD10.8-12.0 in black with its scale on the left y-axis. The dots along the black line indicate the results from the SEVIRI algorithm along the aircraft flight with green, blue, and red denoting clear, cloud, and aerosol, respectively. **(b)** SEVIRI BTD10.8-12.0 again in black along with 0.6 µm reflectivity in blue with its scale on the y-axis from 0 to 50 %. **(c)** SEVIRI RGB image on 16 May at 15:00 UTC with the intricate BAe146 aircraft flight track shown in white. The BAe146 aircraft took off in southeast England (52.1° N, 0.3° W) at approximately 12:55 UTC and landed in northwestern France (47.7° N, 2.1° W) at about 18:10 UTC.

AMTD
6, 5577–5619, 2013

The identification of volcanic ash using the MSG SEVIRI

A. R. Naeger and
S. A. Christopher

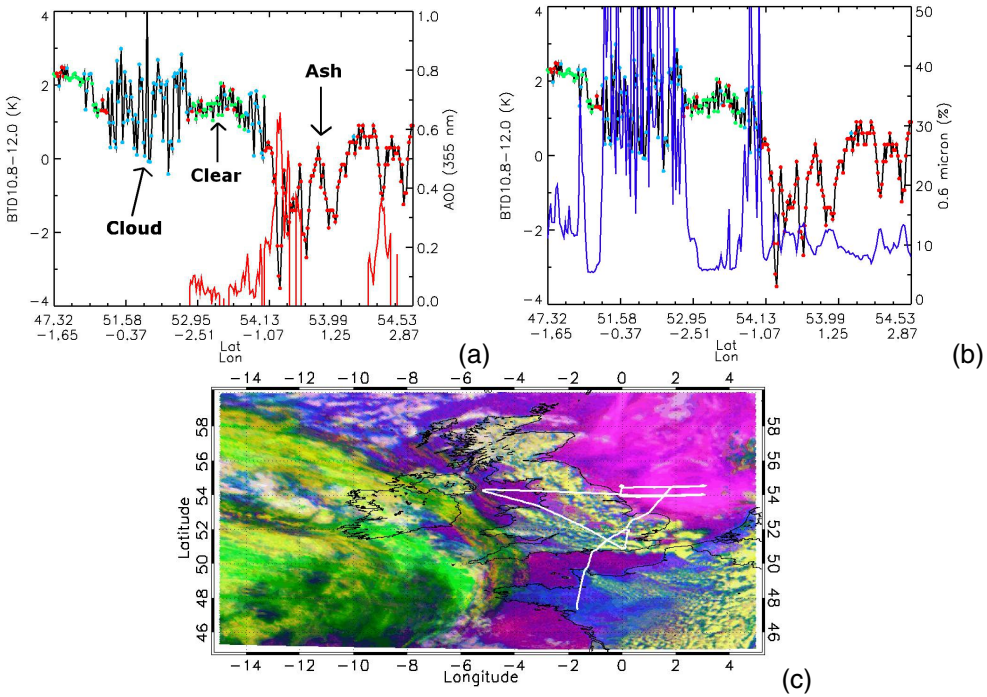

Fig. 7.
(a)–(b) are the same as panels a and b in Fig. 6 except the aircraft AOD and SEVIRI measurements from 17 May are shown here. **(c)** The 17 May BAe146 aircraft flight is overlaid in white on the SEVIRI RGB image from 14:00 UTC where the aircraft took off in northwestern France at 11:26 UTC and landed in southeast England at 16:58 UTC.

AMTD
6, 5577–5619, 2013